Development of a non-linear curvature wavefront sensor for the Subaru Telescope's AO3k system

K Ahn, O Guyon, J Lozi, S Vievard, V Deo, M Lallement, J C Bragg

AO4ELT7 - June 2023 - Avignon

Development of a non-linear curvature wavefront sensor for the Subaru Telescope's AO3k system

K. Ahn[a], O. Guyon[a,b,c,d], J. Lozi[a], S. Vievard[a,d], V. Deo[a], M. Lallement[a,e], and J. C. Bragg[a,c]

[a]Subaru Telescope, National Astronomical Observatory of Japan, National Institutes of Natural Sciences (NINS), 650 North A'ohōkū Place, Hilo, HI 96720, United States
[b]Steward Observatory, University of Arizona, Tucson, AZ 87521, United States
[c]College of Optical Sciences, University of Arizona, Tucson, AZ 87521, United States
[d]Astrobiology Center of NINS, 2 Chome-21-1, Osawa, Mitaka, Tokyo, 181-8588, Japan
[e]Observatoire de Paris, LESIA, 5 Place Jules Janssen, 92190 Meudon, France

ABSTRACT

A few years ago, we started upgrading AO188 into AO3k, including the real-time control system, laser guide star system, deformable mirror (DM), and wavefront sensors (WFSs). In this paper, we present the development of a non-linear curvature WFS (nlCWFS) as a new visible WFS for the upgraded AO3k system. We also introduce the optical and optomechanical design of the nlCWFS. The nlCWFS has two new features: one is the dual-stroke linear mode, and the other one is to deploy non-linear wavefront reconstruction. The dual-stroke linear mode provides a good sensitivity for both low- and high-order aberrations. Also, the non-linear wavefront reconstruction provides a large dynamic range. By combining the linear and non-linear methods, the nlCWFS takes both advantages. Finally, we present laboratory demonstration results of closed-loop experiments in the lab with linear and non-linear wavefront reconstruction algorithms.

Keywords: Adaptive optics, wavefront sensing, phase diversity, wavefront reconstruction

1. INTRODUCTION

The non-linear curvature wavefront sensor (nlCWFS) is a new visible high-order WFS for the AO3k system[5]. The main goal of nlCWFS is to overcome the limitation of the current visible WFS of AO188[7] and provide

Further author information: (Send correspondence to K.A.)
K.A.: E-mail: kyohoon@naoj.org, Telephone: +1(808)-202-1095

extreme adaptive optics (ExAO) performance (Strehl ratio $< 80\%$ in H-band with the median seeing condition) combined with a new ALPAO 64x64 deformable mirror (DM). The current visible WFS can only measure up to 188 modes because it is based on 188 Avalanche photodiodes (APDs)[12]. This number of modes is insufficient for the new DM, which can control more than 3,000 modes. To overcome this limitation, we deploy a quantitative CMOS (qCMOS) camera from Hamamatsu instead of using APDs. We designed the nlCWFS to have 128 pixels across the pupil to run the camera at ∼2 kHz. Consequently, the nlCWFS can measure up to 16,384 (128×128) modes at 2 kHz since a single pixel of the CWFS can measure one mode. The detailed design of the nlCWFS is presented in Sect. 2. Also, the nlCWFS has two new features compared to the conventional CWFS. The first one is that the nlCWFS uses four defocused pupil planes[3], while the traditional CWFS uses only two defocused pupil planes[10]. This allows the nlCWFS to have better sensitivity in both low- and high-order aberrations compared to the conventional CWFS. Figure 1 shows intensities with atmospheric turbulence at different defocused distances. The *top row* shows the cross-section of the pupil images, and the *bottom row* shows example images at near-pupil planes (dz_1) and far-pupil planes (dz_2). Figure 2 shows how a single spatial frequency aberration at the pupil creates intensity modulations in the nlCWFS. The intensity modulation from near-pupil images ($I_{+dz_1} - I_{-dz_1}$) has good sensitivity with a high spatial frequency; in contrast, the intensity modulation from the far-pupil images ($I_{+dz_2} - I_{-dz_2}$) has a good sensitivity with a low spatial frequency, as shown in Figure 2. The other new concept is to deploy the non-linear wavefront reconstruction. The performance of the conventional CWFS is strongly constrained by the requirement that the wavefront sensor signal must be a linear function of the input wavefront aberrations. However, this limitation can be overcome using non-linear wavefront reconstruction, allowing the nlCWFS to have an extensive dynamic range and decent sensitivity. For non-linear wavefront reconstruction, phase retrieval algorithms can be used[2, 6]. In this paper, we use a Gerchberg-Saxton (GS) algorithm[1], which is most commonly used for many phase retrieval applications. The GS algorithm is relatively simple to implement and robust. However, it requires a few iterations to converge, which takes more time. To overcome this drawback of the GS algorithm, we deploy a machine learning (ML) approach for non-linear reconstruction since it doesn't require iterations. Also, ML algorithms have been developed and applied recently to phase retrieval and wavefront sensing in many different fields, including astronomy[8, 9, 13]. These non-linear reconstruction methods are discussed in Sect. 3. In Sect. 4., we also present the first lab demonstration of the nlCWFS and closed-loop test results with linear and non-linear algorithms.

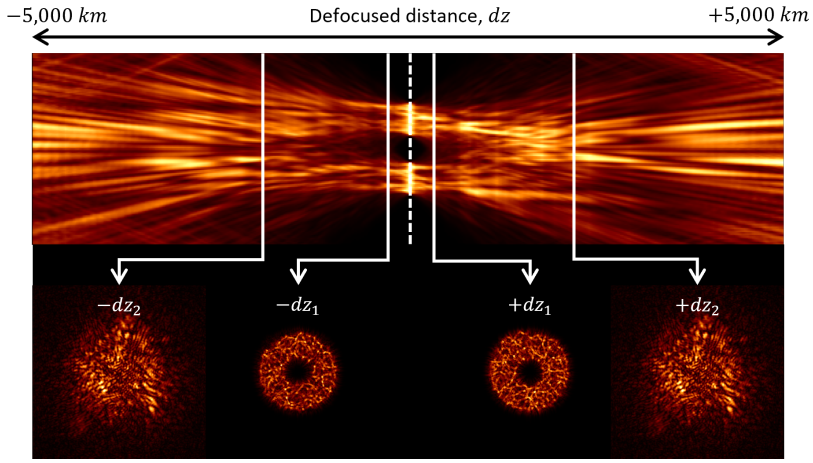

Figure 1. *Top row*: The cross-section of intensities with atmospheric turbulence at different defocused distances. *Bottom row*: Example intensities at near-pupil planes(dz_1) and far-pupil planes(dz_2) with atmospheric turbulence.

2. OPTICAL AND OPTOMECHANICAL DESIGN

Before designing the nlCWFS, we first set a few essential parameters, such as the number of pixels across the pupil (128 pixels), the defocused distances of the pupil ($dz_1 = 100\ km, dz_2 = 1,700\ km$), and the field of view of the WFS (4"). The number of pixels was determined for the maximum frame rate of 2 kHz. The defocus distances were set to preserve a linear relationship between WFS signals and the input phase and to minimize

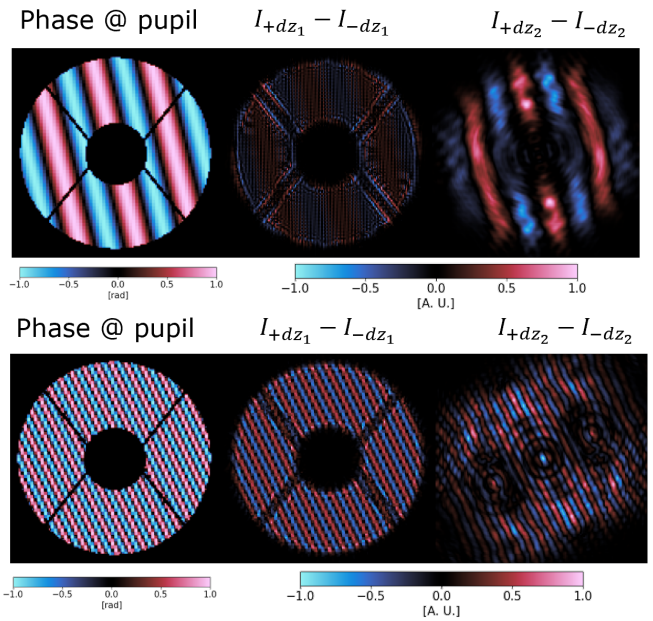

Figure 2. Intensity modulations are created by a single spatial frequency aberration at the pupil. Intensity modulation from near-pupil images ($I_{+dz_1} - I_{-dz_1}$) and far-pupil images ($I_{+dz_2} - I_{-dz_2}$) with a low (*top row*) and high (*bottom row*) spatial frequency at the pupil.

the number of pixels[3]. Also, the defocused distance affects the size of the WFS. However, the beam size on the WFS is only 4 mm, so the defocused distance can be scaled down to approximately 400 mm from the 1,700 km with an 8 m telescope pupil size thanks to the Fresnel number equation. Therefore, we can make the WFS system reasonably compact. Lastly, the field of view restrains the size of optics and optomechanical parts. We use some flat mirrors of 2 inches to meet the 4" field of view, which is identical to the current CWFS.

While the current CWFS uses a vibrating membrane to make the defocused pupil images at different locations, the nlCWFS uses two beam splitters (BS) or two dichroic filters to generate four defocused pupil images on a single detector simultaneously. Figure 3 shows the proposed optical design for the nlCWFS. Also, four different optical paths are illustrated in Figure 3. In Figure 3 *right*, the dotted lines indicate the conjugated planes to the camera through the imaging lens, and the solid lines indicate the actual pupil positions imaged by pupil re-imaging lenses. Finally, we can have four defocused pupil images simultaneously from these different optical paths.

Also, Figure 4 shows the optomechanical design for the nlCWFS. We designed the nlCWFS to be installed above the current CWFS due to the lack of space inside AO188 currently. Due to this reason, we use the pickoff BS with 90% reflection and 10% transmission to pick up the light from the current CWFS. This feature allows us to use two WFSs simultaneously, and then we can compare the AO performance between the current CWFS and the nlCWFS. This pickoff BS is mounted on a motorized linear stage so that it can be moved out when it's not used. For better stability of the nlCWFS system, we use four 1.5-inch diameter posts and the support plate under the breadboard of the nlCWFS. After the pickoff BS, folding mirrors (FMs) are used to send the light to other optical elements. The initial beam size from the current CWFS is 5 mm, but we reduce the beam size to 4 mm using pupil re-imaging lenses ($L1$, $f = 500\ mm$ and $L2$, $f = 400\ mm$ in Figure 4). There are also two rotation stages (RSs) with three different optical elements (dichroic filter, polarizing BS (PBS), Mirror) for three modes, such as a natural guide star (NGS) mode, a laser guide star (LGS) mode, a focal plane wavefront sensing (FPWFS) mode. The NGS mode uses two dichroic filters to have four defocused pupil images, and each defocused pupil image has a different wavelength range. The LGS mode uses two PBSs and a half-wave plate to have only two near-pupil images. The FPWFS mode uses two mirrors and an imaging lens ($L3$), and then the light will be focused on the detector instead of looking at the defocused pupil image. This mode will be used for faint targets with phase diversity algorithms. In addition, the $FM4$ and $FM5$ are mounted on the linear stage, and the $FM8$

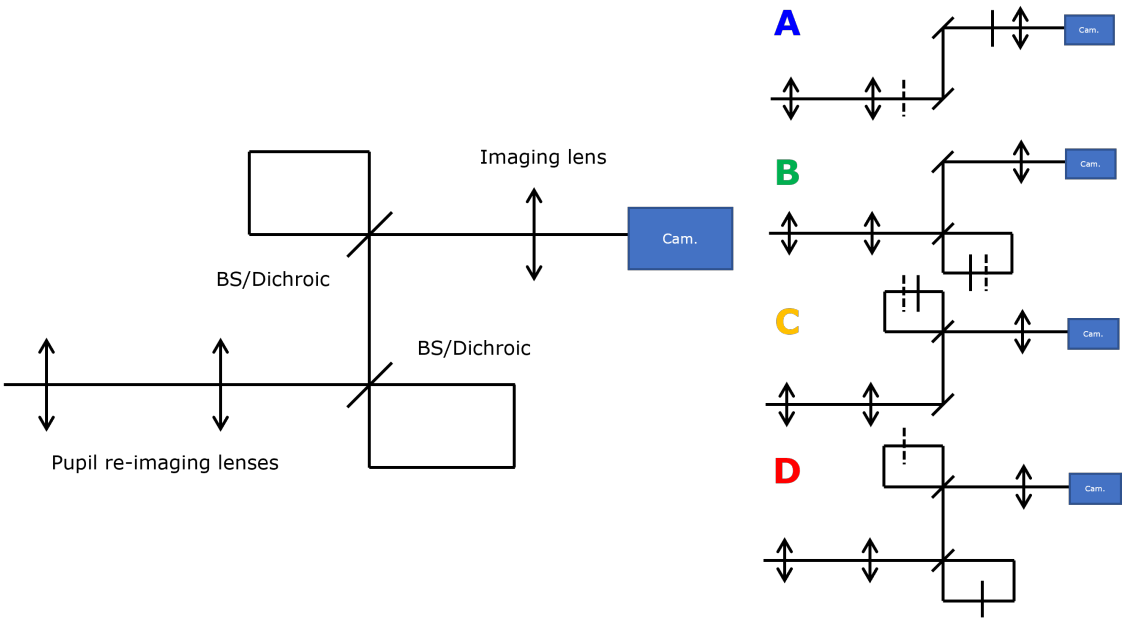

Figure 3. Optical layout (*Left*) and four possible optical paths (*right*) for the nlCWFS. The dotted lines indicate the conjugated planes to the camera through the imaging lens, and the solid lines indicate the actual pupil positions imaged by pupil re-imaging lenses.

and $FM9$ are mounted on the linear stage separately. So, we can adjust the defocused distance for near-pupil images depending on the seeing condition.

3. RECONSTRUCTION ALGORITHMS

3.1 Linear algorithm

We implement the modal control mode of the CACAO package[4] for the linear control mode. The required DM command α in the closed-loop can be briefly written as:

$$\alpha = \mathbf{C}\Delta I, \tag{1}$$

with $\mathbf{C}$ the pseudo-inverse of the response matrix $\mathbf{R}$, ΔI the intensity difference between the reference intensity and aberrated intensity. During the calibration process, the response matrix is measured as:

$$\mathbf{R} = \begin{pmatrix} | & & | \\ \Delta I_1 & \dots & \Delta I_N \\ | & & | \end{pmatrix}, \tag{2}$$

$$\Delta I_i = \frac{I_i^+ - I_i^+}{2a_p}, \tag{3}$$

with I_i^+ and I_i^- the flattened wavefront sensor intensities for positive and negative actuations of the ith mode, respectively, and ΔI_i the subsequent differential intensity response to the ith mode. We then compute the control matrix ($\mathbf{C}$) by inverting the response matrix using singular value decomposition (SVD). In the actual implementation, we measure two response matrices, one with two near-pupil images and the other one with four defocused pupil images. We then apply different modal cutoff points for two control matrices to select the number for control modes. We set a lower cutoff for the control matrix with two near-pupil images to have enough modes for correcting high-order modes. In contrast, we set a higher cutoff to the control matrix with four defocused pupil images only for correcting the low-order modes.

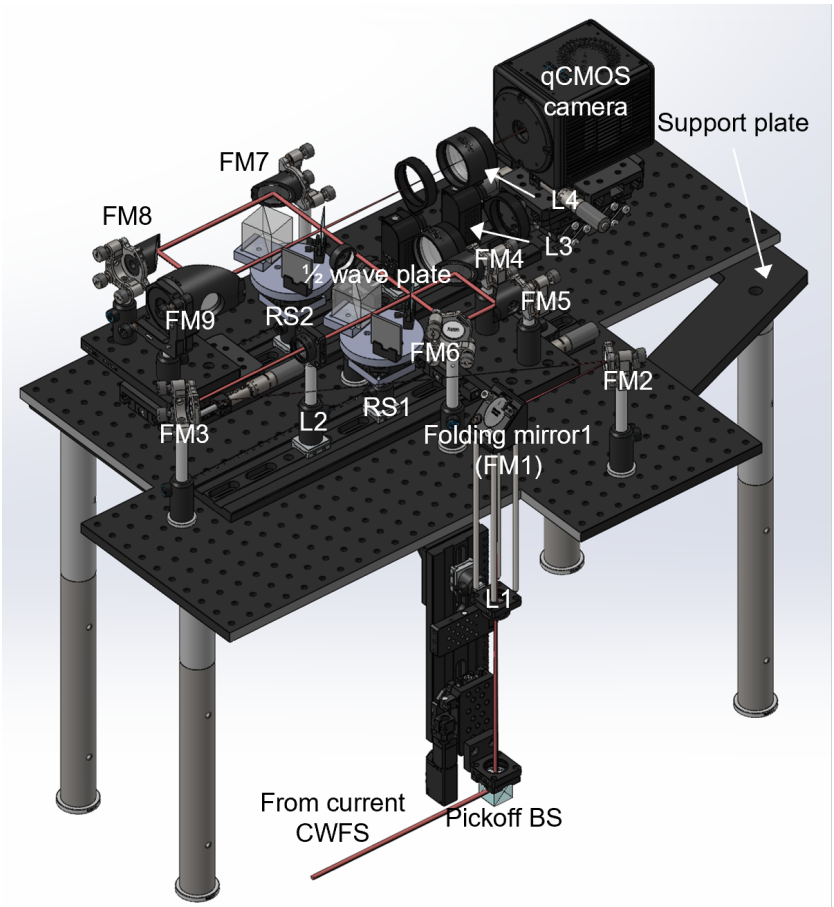

Figure 4. Optomechanical design for the nlCWFS. FM: folding mirror, L: lens, RS: rotation stage, BS: beam splitter.

3.2 Non-linear algorithm

As mentioned in Sect. 1, the GS algorithm is used in this paper for non-linear reconstruction, but many other options and variations on the algorithm are available. The algorithm used for this paper is illustrated in Figure 5. The output of the GS algorithm is a wrapped phase, so the phase unwrapping process is required after the GS algorithm. We use Zernike polynomials for the phase unwrapping[2], as shown in Figure 5. The phase slope is insensitive to phase wrapping effects, as it is here computed as the difference between the phase of adjacent pixels, and any value above $+\pi$ or below $-\pi$ is brought back in the $-\pi$ to $+\pi$ interval by adding or subtracting 2π. The resulting phase slope is decomposed as a linear sum of precomputed phase slopes of Zernike polynomials. The coefficients of this decomposition are the Zernike coefficients of the unwrapped phase, which can be reconstructed as a sum of Zernike polynomials. This process is a simple matrix-vector-multiplication, so it can be done in real-time.

Also, we deploy the ML approach for non-linear reconstruction. A large and representative labeled data set for training is essential for the success of deep learning. However, we only use one data set consisting of 10,000 frames of input phase and four defocused pupil images from the WFS since our work is primarily motivated to validate the feasibility of the ML approach. To generate the data set, we simulate the Kolmogorov turbulence with 0.5" seeing for the input phase and put this phase map onto the spatial light modulator (SLM). At the same time, we record the wavefront sensor frames. Figure 6 shows a single frame of the data set. There are a number of neural network (NN) architectures for image classification applications, but we only use U-Net[11], which has shown promising results in previous research[8]. For the training, we use the root-mean-square error (RMSE) between the input and output phases.

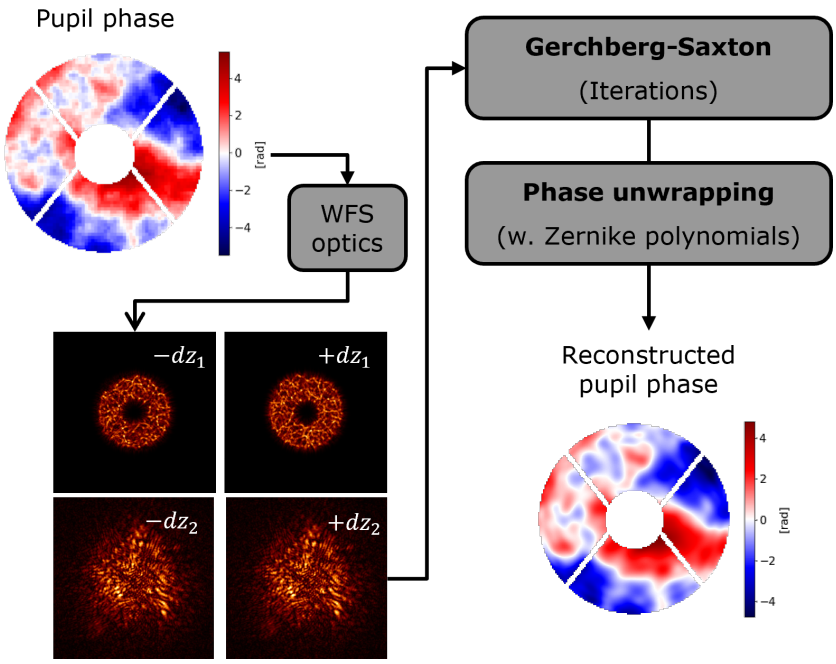

Figure 5. A schematic diagram of the GS algorithm, including phase unwrapping.

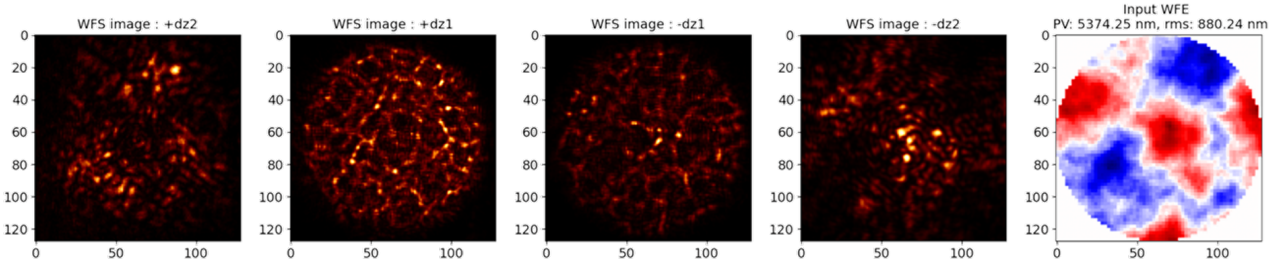

Figure 6. An example frame of the data set for the NN training.

4. LABORATORY DEMONSTRATION

Figure 7 shows the actual setup in the lab for closed-loop tests. We use a He-Ne laser with a 632.8 nm wavelength. The laser beam is collimated by the lens in front of the laser and then reflected by the SLM. We use the SLM for injecting both the turbulence and correction. This SLM from Meadowlark Optics has 512×512 actuators, but we only use 320 pixels across the clear aperture of the pupil mask to match the actual beam size of the current WFS. We are binning (5×5) the actuators to simulate the ALPAO's 64×64 DM, which will be used for the AO3k system. Also, we installed a linear polarizer after the SLM to match the polarization direction after the collimating lens.

Figure 8 shows the software setup for the lab demo. The *top left* window shows the wavefront sensor image (128×512), the *top middle* window is the total SLM command, which is the residual errors, and the *top right* window is the viewer for the point spread function (PSF) monitoring camera. The *bottom left* is a terminal to run Python scripts for testing, and the *bottom right* window is 12 software channels to write the SLM commands so that we can use them independently. In our demonstrations, we used two or three channels to apply the turbulence, the correction from the linear reconstructor, and the correction from the non-linear reconstruction.

We first compared AO performance with two near-pupil images like conventional CWFS and with four defocused pupil images (near- and far-pupil images). Figure 9 (*left*) shows residual wavefront errors (WFEs) with two near-pupil images (2 planes) and with four defocused pupil images (4 planes). We noticed that the AO performance with 4 planes has faster convergence and smaller residual errors, as shown in Figure 9 (*left*). Also, Figure 9 (*right*) shows the power spectral density (PSD) of the residual errors. It clearly shows the closed loop

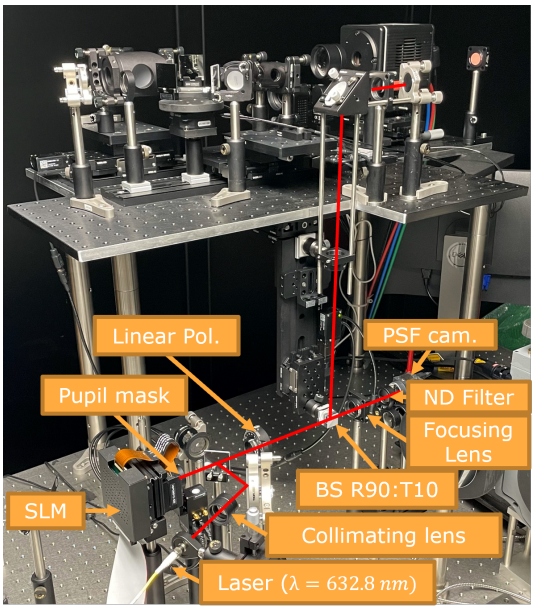

Figure 7. Actual setup in the lab for the closed-loop tests.

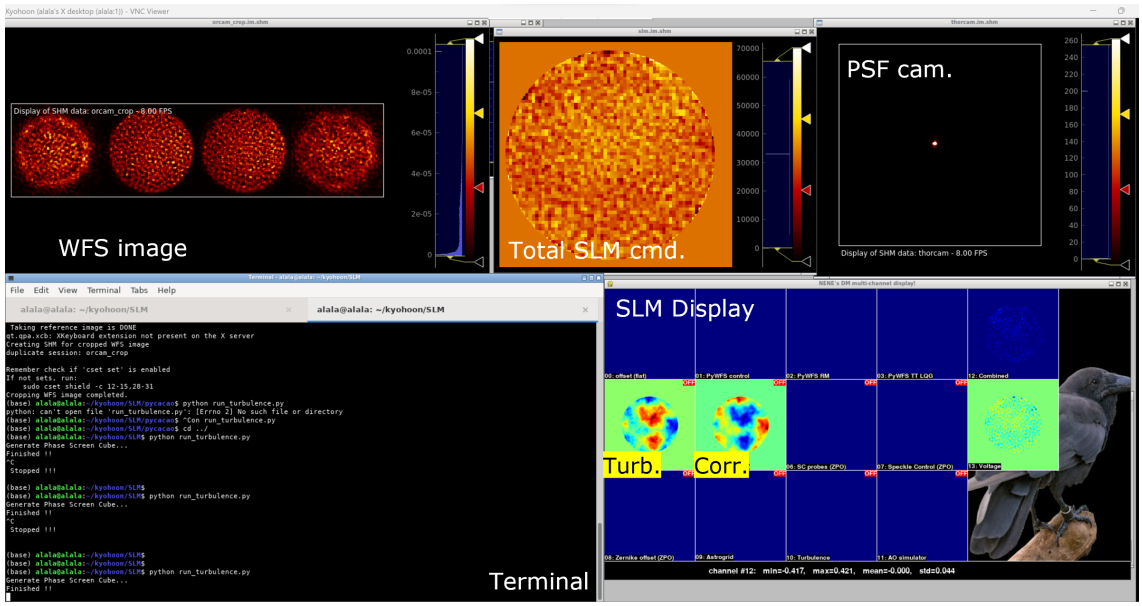

Figure 8. Software setup for the lab demo. *Top left*: Wavefront sensor image viewer, *top middle*: The total SLM command, *top right*: the viewer for the PSF monitoring camera. *Bottom left*: a terminal to run Python scripts, and *Bottom right*: 12 software SLM channels.

with 2 planes has a better correction in higher modes, and the closed loop with 4 planes has a better correction in lower modes. However, our final idea for closing the loop on-sky with linear reconstructors is to close the AO loop with 2 planes first and then close the AO loop with 4 planes once the WFE gets smaller.

For non-linear reconstructions, we combine them with linear reconstructions for better loop stability. The idea is to bootstrap the wavefront error with non-linear reconstructions at the beginning of the AO loop, and once the wavefront error gets into the linear regime, we then change the reconstructor to the linear reconstructor. Figure 10 shows the RMS WFE (*left*) with different reconstructions and the Strehl ratios (*right*) as a function of the magnitude of the target. We confirmed that both the linear and non-linear reconstructors show stable closed-loop performance over 5,000 iterations. The non-linear reconstructor with NN shows the fastest convergence compared

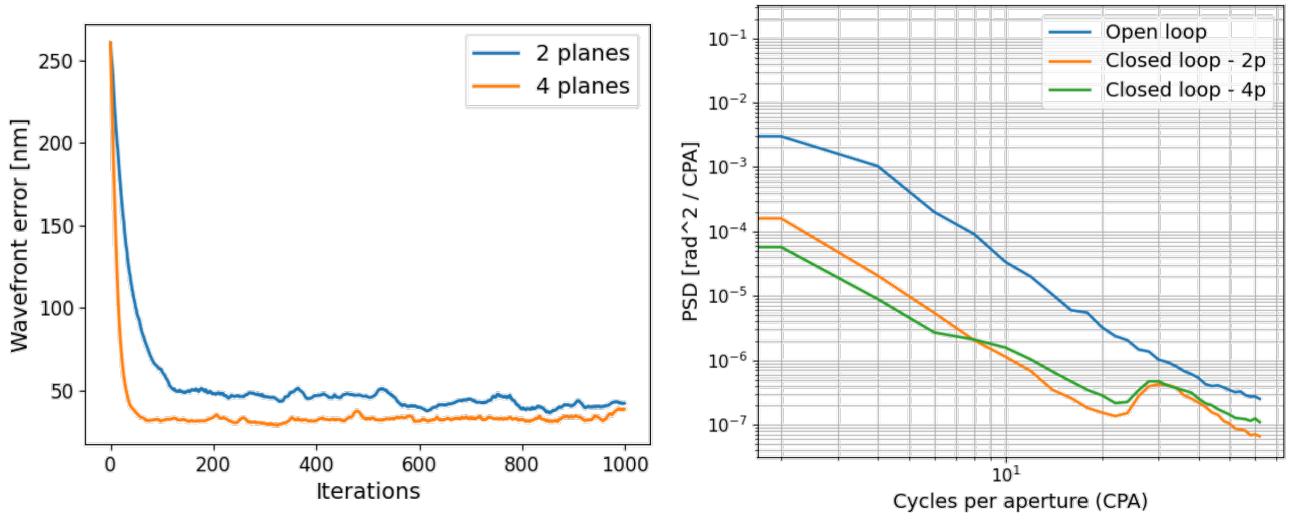

Figure 9. *Left*: WFEs with two near-pupil images (*blue line*) and with four defocused pupil images (*orange line*). *Right*: PSD of the residual errors. The *blue line* is an open loop, the *orange line* is with 2 planes, and the *blue line* is with 4 planes.

to other methods. Also, all methods showed a significantly improved Strehl ratio with reasonably bright stars ($m_V > 14$) compared to the current AO188's performance.

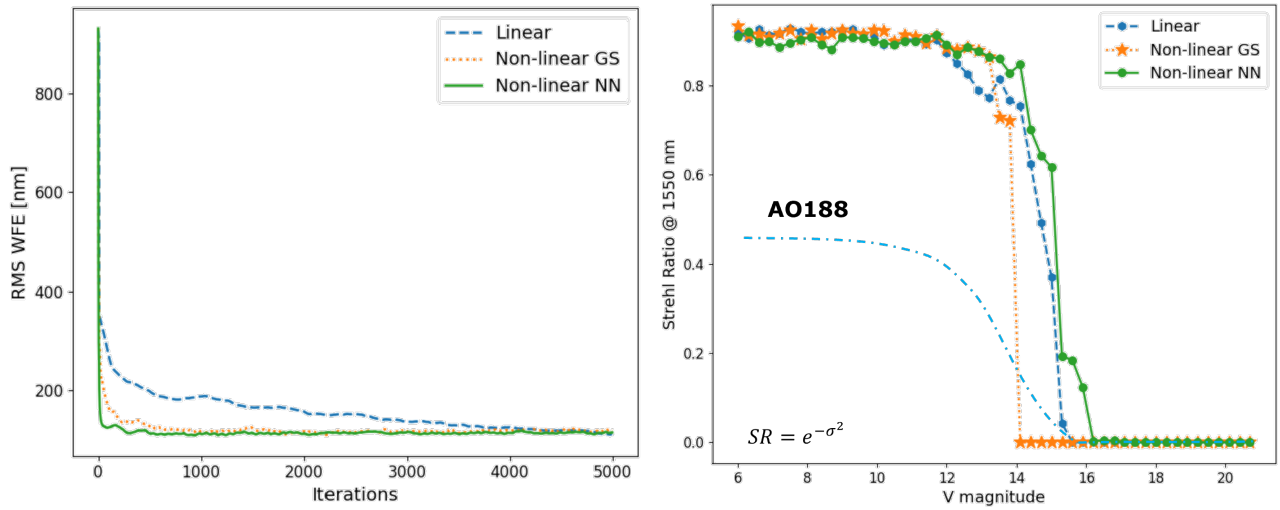

Figure 10. Residual WFE (*left*) with different reconstructions and SR (*right*) as a function of the magnitude of the target.

5. SUMMARY AND FUTURE WORKS

We presented the development of the nlCWFS for Subaru's new AO3k system, which offers ExAO correction to all science instruments downstream of AO3k. We showed the optical and optomechanical design of the nlCWFS to have four defocused pupil images on a single detector simultaneously. We also showed the laboratory demonstration of the nlCWFS and closed-loop tests with the SLM. In the lab demo, we implemented closed-loop tests with both linear and non-linear reconstructors and compared the performance. The linear reconstructor with 4 planes showed better performance compared to the linear reconstructor with 2 planes, which is identical to the conventional CWFS method. Moreover, combining the linear reconstructors and non-linear reconstructors showed very promising results and better performance than the *linear-only* mode. From these results, we confirmed that

we could compensate for the aberration with a large amplitude thanks to the non-linear reconstructor's extensive dynamic range and keep the AO loop stable using the linear reconstructors.

For future works, we will commission the nlCWFS with Subaru Telescope soon and conduct on-sky engineering tasks to validate the performance. Also, we will test the nlCWFS with the new 64×64 DM once we have it. In the meantime, we will work on improving the computation speed of non-linear algorithms to be able to use these for actual AO loops. Additionally, we will conduct more tests for the ML method, for example, with different NN architectures, number of data, seeing conditions, flux levels, and so on. We anticipate these will make the non-linear reconstruction with NN more robust and stable.

ACKNOWLEDGMENTS

This work is based on data collected at Subaru Telescope, which is operated by the National Astronomical Observatory of Japan. The authors wish to recognize and acknowledge the very significant cultural role and reverence that the summit of Maunakea has always had within the Hawaiian community. We are most fortunate to have the opportunity to conduct observations from this mountain. The authors also wish to acknowledge the critical importance of the current and recent Subaru Observatory daycrew, technicians, telescope operators, computer support, and office staff employees. Their expertise, ingenuity, and dedication is indispensable to the continued successful operation of these observatories. The development of SCExAO was supported by the Japan Society for the Promotion of Science (Grant-in-Aid for Research #23340051, #26220704, #23103002, #19H00703 & #19H00695), the Astrobiology Center of the National Institutes of Natural Sciences, Japan, the Mt Cuba Foundation and the director's contingency fund at Subaru Telescope. KA acknowledges support from the Heising-Simons Foundation.

References

[1] GW Gerchberg and WO Saxton. "A practical algorithm for the determination of the phase from image and diffraction plane pictures". In: *Optik* 35 (1972), pp. 237–246.

[2] Olivier Guyon. "High sensitivity wavefront sensing with a nonlinear curvature wavefront sensor". In: *Publications of the Astronomical Society of the Pacific* 122.887 (2009), p. 49.

[3] Olivier Guyon et al. "Improving the sensitivity of astronomical curvature wavefront sensor using dual-stroke curvature". In: *Publications of the Astronomical Society of the Pacific* 120.868 (2008), p. 655.

[4] Olivier Guyon et al. "The compute and control for adaptive optics (CACAO) real-time control software package". In: *Adaptive Optics Systems VI*. Vol. 10703. SPIE. 2018, pp. 469–480.

[5] Julien Lozi et al. "AO3000 at Subaru: Combining for the first time a NIR WFS using First Light's C-RED ONE and ALPAO's 64x64 DM". In: *Adaptive Optics Systems VIII*. Vol. 12185. SPIE. 2022, pp. 991–1004.

[6] Mala Mateen. "Development and verification of the non-linear curvature wavefront sensor". PhD thesis. The University of Arizona, 2015.

[7] Yosuke Minowa et al. "Performance of Subaru adaptive optics system AO188". In: *Adaptive Optics Systems II*. Vol. 7736. SPIE. 2010, pp. 1302–1308.

[8] Gilles Orban De Xivry et al. "Focal plane wavefront sensing using machine learning: performance of convolutional neural networks compared to fundamental limits". In: *Monthly Notices of the Royal Astronomical Society* 505.4 (2021), pp. 5702–5713.

[9] Quesnel, M. et al. "A deep learning approach for focal-plane wavefront sensing using vortex phase diversity". In: *A&A* 668 (2022), A36. DOI: 10.1051/0004-6361/202143001. URL: https://doi.org/10.1051/0004-6361/202143001.

[10] Francois Roddier. "Curvature sensing and compensation: a new concept in adaptive optics". In: *Applied Optics* 27.7 (1988), pp. 1223–1225.

[11] Olaf Ronneberger, Philipp Fischer, and Thomas Brox. "U-net: Convolutional networks for biomedical image segmentation". In: *Medical Image Computing and Computer-Assisted Intervention–MICCAI 2015: 18th International Conference, Munich, Germany, October 5-9, 2015, Proceedings, Part III 18*. Springer. 2015, pp. 234–241.

[12] Makoto Watanabe et al. “Implementation of 188-element curvature-based wavefront sensor and calibration source unit for the Subaru LGSAO system”. In: *Adaptive Optics Systems*. Vol. 7015. SPIE. 2008, pp. 1727–1734.

[13] Alison P Wong et al. “Machine learning for wavefront sensing”. In: *Adaptive Optics Systems VIII*. Vol. 12185. SPIE. 2022, pp. 791–809.